RESEARCH PAPER

Commissioning observations of HD 189733 with the PAlomar Radial Velocity Instrument

Bryson L. Cale [a,b,*] Aurora Kesseli,[b] Charles Beichman,[a,b] Gautam Vasisht,[a]
Rose K. Gibson,[c,d] Rebecca Oppenheimer [d] Jason Fucik,[e] Dimitri Mawet,[e]
Christopher Paine,[a] Kittrin Matthews [a] Thomas Lockhart,[a] Samuel Halverson [a]
Boqiang Shen [e] Mahmood Bagheri,[a] Stephanie Leifer [e] Peter Plavchan [f]
and David Hover[e]

[a]Jet Propulsion Laboratory, California Institute of Technology, Pasadena, California, United States
[b]IPAC, Pasadena, California, United States
[c]Columbia University, New York, New York, United States
[d]American Museum of Natural History, New York, New York, United States
[e]California Institute of Technology, Pasadena, California, United States
[f]George Mason University, Fairfax, Virginia, United States

ABSTRACT. The PAlomar Radial Velocity Instrument (PARVI) is a diffraction-limited, high-resolution spectrograph connected by single-mode fiber to the 200 inch Hale telescope at Palomar Observatory. Here, we present on-sky results for HD 189733 obtained during PARVI's commissioning phase. We first describe the implementation of our spectral extraction and radial velocity (RV) generation codes. Through RV monitoring, we detect the Rossiter–Mclaughlin signal of the transiting planet HD 189733 b. We further detect the presence of water and carbon monoxide in the atmosphere of HD 189733 b via transmission spectroscopy. This work demonstrates PARVI's high-resolution spectral capabilities at H band and current intra-night Doppler stability of $\sim$4 to 10 m s^{-1} on an early K dwarf. Finally, we discuss the limitations to this work and ongoing efforts to characterize and improve the Doppler performance of PARVI to the design goal of $\sim$1 m s^{-1} for late-type stars.

1 Introduction

From the initial discoveries of a few hundred planets via the radial velocity (RV) technique to the discovery of thousands of confirmed and candidate exoplanets by the transit missions Kepler and TESS, the field of exoplanets has exploded within the last two decades. The confirmation of transiting exoplanets requires follow-up with RV observations to independently confirm the existence of the planet and measure the orbital eccentricity and the dynamical mass of the planet (and therefore infer its composition). A precision of 20% for the mass determination is recommended for enabling detailed atmospheric characterization, particularly for terrestrial-mass planets.[1] The discovery and characterization of Earth-sized planets requires the development of extreme precision RV instruments as described in a recent study by the National Academy of Sciences.[2] To address these challenges, new spectrographs from the visible to near-infrared (NIR) wavelengths are being developed using a variety of innovative technologies.

*Address all correspondence to Bryson L. Cale, bryson.cale1@gmail.com

The PAlomar Radial Velocity Instrument (PARVI) is an NIR (J and H band) spectrograph designed to operate at the 200 inch Hale telescope at Palomar Observatory. A unique aspect of PARVI's design is that the Palomar adaptive optics (AO) system feeds light into the spectrograph via a single-mode fiber (SMF). Unlike multi-mode fibers used with seeing-limited spectrographs, an SMF feed provides several advantages, including a dramatically smaller spectrograph, immunity to seeing variations at the entrance aperture, and it dramatically reduces modal noise.

In this work, we present results from commissioning observations of HD 189733 with PARVI. We briefly describe the instrument (Sec. 2) and the implementation of our spectral extraction (Sec. 3) and RV generation codes (Sec. 4). In Sec. 5.1, we demonstrate the current Doppler performance of PARVI with the detection of the Rossiter–Mclaughlin (RM) signal of the well-known transiting planet HD 189733 b and find consistent results with previous observations. In Sec. 5.2, we find evidence for water and carbon monoxide in the atmosphere of HD 189733 b via transmission spectroscopy, also consistent with previous detections. We conclude with a discussion of limitations of our analyses and ongoing commissioning work to improve the performance of PARVI in Sec. 6.

2 PARVI Instrument

PARVI is a cross-dispersed NIR spectrograph fed by a SMF from the Palomar PALM-3000 (P3K) AO system. The benefit of an SMF feed is that the spectrograph size is dictated only by the desired spectral resolution and the wavelength and not by the size of the telescope and the seeing disk. In the case of PARVI, the designed resolution of $R = 87,000$ to $121,000$ is achieved with an input beam of 25 mm and a grating size (long dimension) of ∼11 cm. Unlike with seeing-limited spectrometers, in a diffraction limited spectrometer, the re-imaged slit width is the diffraction limited point spread function (PSF) width, which linearly scales with wavelength. An $R4$ grating with 13.6 lines mm^{-1} and a silicon prism cross-disperser image 46 spectral orders ($m = 85$ to 130) covering the J and H bands onto an H2RG detector. A second SMF feeds the signal from a laser frequency comb (LFC), which generates hundreds of individual spectral modes spaced by 10 GHz (∼0.08 μm) across each order for a stable wavelength reference (<30 cm s^{-1}; Ref. 3). The layout of PARVI is shown in Fig. 1. A summary of parameters for PARVI is provided in Table 1.

Commissioning at the telescope began in late-2019 but was drastically curtailed by the shutdown and limited access to Palomar during the COVID-19 pandemic. Upgrades and modifications made during this period include the transition from an LN$_2$-cooled cryostat to a closed cycle refrigerator, which has greatly enhanced the thermal stability of the optical system. However, during the commissioning period, we identified a source of wavelength instability due to the interaction between the polarization of the signal with polarization birefringence in the silicon cross-disperser. This effect induces "polarization noise" (e.g., Refs. 4 and 5) and has limited the night-to-night precision on-sky to 10 to 20 m s^{-1}.[6] By tracking individual LFC modes throughout a given night, we have demonstrated a relative internal stability of <1 m s^{-1} between the science and calibration fibers when scrambling light from the LFC.[6] A number of steps are being taken to mitigate this effect for starlight, and we briefly revisit these challenges further in Sec. 6. However, PARVI's current performance was sufficient to carry out the commissioning observations described in this paper.

3 Observations and Pre-processing

We select observations obtained during PARVI's commissioning phase of HD 189733 to demonstrate the performance of PARVI and our data reduction software. HD 189733 is a bright ($H = 5.59$ mag) K2 main sequence dwarf star host to a transiting hot-Jupiter on a ∼2.22-day orbit[7] and has served as a benchmark target for numerous RV programs. We observed HD 189733 on UT dates May 15–18, 2022, including a full-transit on the first night. Exposure times were set to 372 s. We recorded 19 exposures covering the transit + baseline of HD 189733 b, and 4 to 6 exposures on each of the remaining 3 nights. (Additional observing procedures with PARVI using the Palomar PALM-3000 AO system are described in Ref. 8.) As part of a
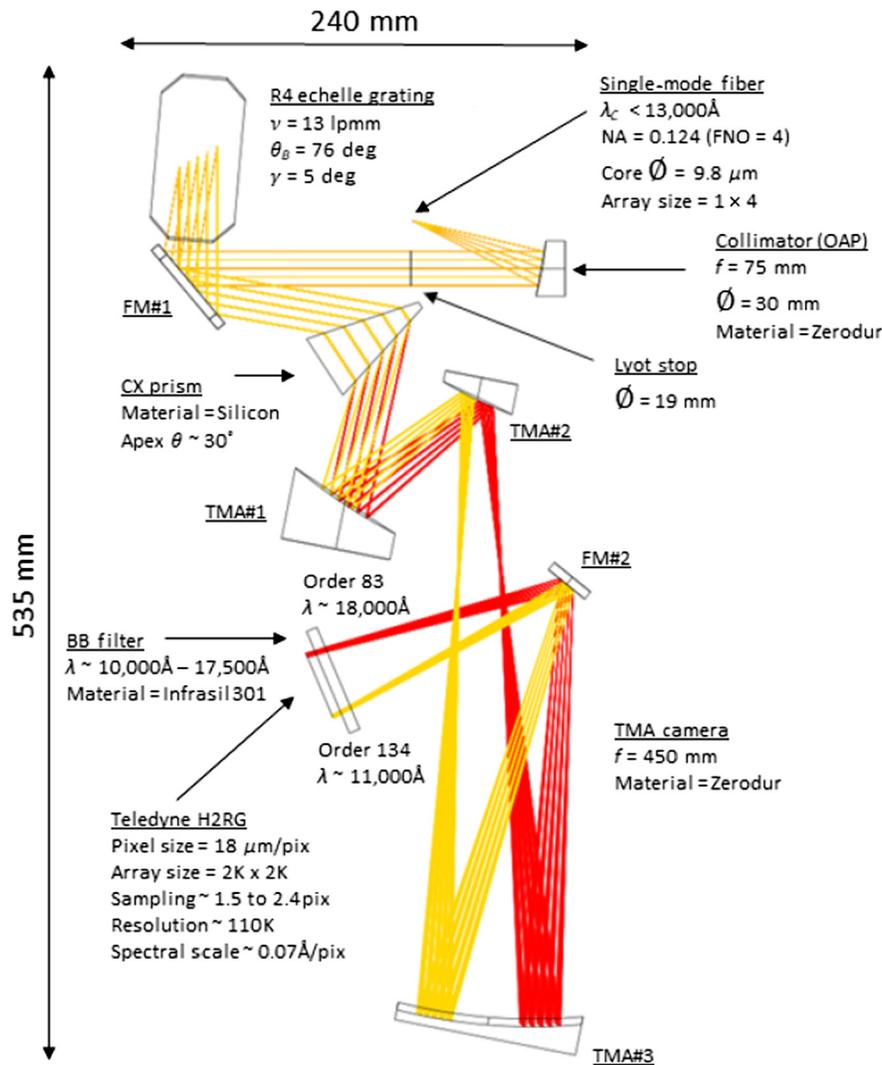
Fig. 1 Schematic showing the layout of the cross-dispersed echelle spectrograph, which is designed to achieve $R \sim 87,000$ to 121,000 in a compact 0.5 m $\times$ 0.25 m optical bench through the use of a SMF input from the Palomar AO system.

commissioning experiment to mitigate the polarization effects, all the observations presented in this work were obtained using an un-coated silicon cross-disperser, which attenuates the signal by a factor of ≈ 2.5 compared to the coated prism. (The coating was removed in April 2022 and reinstalled in February 2023.) The seeing for these observations ranges from 1.2 to 2" and is typical for Palomar Observatory.

Gibson et al.[9] developed methods to optimally extract raw PARVI spectra with algorithms based on the CERES routines.[10] Here, we utilize a second pipeline implemented in the Julia package Echelle.jl (https://github.com/astrobc1/Echelle.jl/), the successor to the Python package pychell.[11] We leave the details of this extraction process to the Appendix. We compare corresponding RVs for the two sets of spectra in Sec. 5.1 and further discuss the extraction of PARVI spectra in Sec. 6.2.

For all exposures of astronomical sources, we also record a simultaneous trace of the LFC spectrum (Ref. 9). Although the LFC can be utilized to provide a unique wavelength solution for each exposure, we choose to use a static wavelength solution for all observations due to ongoing challenges of monitoring changes to the wavelength solution (Refs. 6, 9, and Sec. 2 of this work). We construct a wavelength solution using a process similar to that described in Ref. 9. We utilize 18 consecutive exposures of the LFC recorded in the late afternoon of May 14, 2022 (local time)

Table 1 Summary of PARVI characteristics.

Parameter	Value
λ	1145 to 1766 nm
Diff. limit ($1.22\lambda/D$)	87.5 mas at 1766 nm
Fiber core diameter	9.8 μm = 68.5 mas
LFC pump line, λ_p	HCN at 1559.9 nm
LFC spacing ($\Delta\nu$)	10 GHz (~0.08 nm)
LFC lines per order	~150 to 200
LFC stability	<30 cm s^{-1}
Echelle orders	85 to 130
$R = \lambda/\Delta\lambda$ (designed)	87,000 (red, H band) to 121,000 (blue, J band)
$R = \lambda/\Delta\lambda$ (current)	50,000 to 70,000 (H band only)
$\Delta\lambda$ per order	~15.6 nm at λ_p
$\Delta\lambda$ per pixel	$\Delta\lambda \sim$ 0.008 nm at λ_p
Δ RV per pixel	~1 km s^{-1} at λ_p
Pixel sampling	3.5 pixels per resolution element (H band)
H band image field	24.0 × 19.2 arcsec
Efficiency[a]	2%

[a]Represents the average efficiency achieved using an anti-reflective (AR) coating on the PARVI cross-dis-
perser and will be used in future observations. The average efficiency in this work is reduced by ~40% due
to the absence of the AR coating. We briefly discuss this further in Sec. 3.

with exposure times of 186 s, which are median combined to create a high signal-to-noise ratio (S/N) LFC image. Each extracted (1D) LFC mode is fit using with a model composed of a Gaussian (amplitude, mean, and width) and linear trend to account for the highly chromatic underlying supercontinuum of the LFC. The parameters are optimized with a Levenberg–Marquardt solver implemented in LsqFit.jl,[12] which also provides estimates of the parameter uncertainties via finite-difference techniques. For echelle orders $m = 85$ to 105 ($\lambda = 1401$ to 1754 nm), we then fit the nominal mode positions with a 2D Chebyshev polynomial (e.g., Refs. 10 and 13) of degree 12 in both the "pixel" and "echelle order" dimensions, with weights inversely proportional to the Gaussian-mean uncertainties (squared). For $m > 105$, the LFC modes exhibit low contrast in flux relative to the supercontinuum and are therefore not well-defined. We briefly discuss the utilization of J band orders in Sec. 6. The unweighted root-mean squared (RMS) of the residuals from the 2D fit is ~25 m s^{-1}. An estimation of uncertainty in our wavelength calibration (RMS/$\sqrt{N_{\mathrm{modes}}}$) is ~40 cm s^{-1}.

4 RV Generation

In order to generate RVs from PARVI spectra, we iteratively forward model each observation on a per-order basis using a modified spectral forward model[11] implemented in Echelle.jl. We briefly describe each of the model components in turn. The spectral continuum is modeled with a cubic spline. Seven knots are uniformly spaced across the order and are parameters to be optimized. The full continuum is then generated by interpolating through the knots with a cubic spline.

The telluric spectrum is modeled using templates provided from the Transmissions Atmosphériques Personnalisées pour l'AStronomie (TAPAS).[14] We fit for two power-law scaling factors to account for the variable airmass and variable precipitable water vapor of the

observations. We also fit for a telluric Doppler shift factor to account for variable atmospheric winds and instrumental drifts not accounted for in this work.

For the star, we start with a BT-Settl synthetic stellar template[15] with parameters $T_{\text{eff}} = 5000$ K, $\log g = 4.5$, and Fe/H = 0. The template is further broadened to a $v \sin i = 3$ km s^{-1} using the rotBroad routine from PyAstronomy.[16] Once all observations are fit, we Doppler shift each vector of residuals to a coherent reference frame according to the best-fit Doppler shifts. Each shifted vector of residuals is then resampled onto an oversampled ($\sim$8$\times$) wavelength grid using cubic spline interpolation, which is common to all observations (for this order). The stellar template is then updated (additively) based on the median of these residuals, weighted by RMS^{-2}, where RMS is the unweighted root mean square of the spectral model fit. This process is repeated for eight iterations, although the RVs have converged by iteration $\sim$5. Most likely due to uncharacterized changes in the wavelength solution, RVs for nights 2 to 4 are offset and are therefore not included in additional analyses. However, so long as changes to the wavelength solution are primarily achromatic (in velocity), these observations still increase the achieved S/N of the data-driven stellar template and are therefore included at this step. The precision of the corresponding RV measurements on these nights may also reflect PARVI's precision for a single exposure.

To account for the line spread function (LSF) of the 1D spectrum, we apply a Gaussian model with a width unique to each echelle order, but identical for all exposures, which is an adequate assumption given the expected stability of SMFs. The width of the Gaussian is determined by the width of the LFC modes as measured in Sec. 3. Due to PARVI's compact construction, the off-axis angle of the echelle grating is larger than for other high resolution echelle spectrographs. This causes spectral features on the detector to appear tilted along the dispersion axis (Fig. 2). The tilt of LFC modes is also strongly chromatic within an order (Fig. 3). We approximate the effective LSF width for a given order as the median value from all fits across the order. We further discuss the optimal LSF for PARVI in Sec. 6.2.

The spectral forward model is optimized using an Iterative Nelder–Mead algorithm (https://github.com/astrobc1/IterativeNelderMead.jl), which also provides an estimation of the parameter uncertainties through finite difference techniques. Due to the ongoing characterization and improvements to processing PARVI data products, we generate RVs for spectra of HD 189733 extracted and calibrated with the processes described in this work (Sec. 3), and the same spectra processed using methods outlined in Ref. 9, both utilizing a static LSF.

We generate RVs for orders $m = 85$ to 105; however, orders $m = 100$ to 105 are dense with telluric features from water in Earth's atmosphere and yielded RVs which are inconsistent with other orders so we discard these orders before coadding RV measurements. We further discard order $m = 85$, which is inconsistent with the remaining orders. We suspect this is due to the order being an endpoint in constructing the wavelength solution (Sec. 3) and is therefore not well constrained. To combine RVs from different echelle orders, we first subtract the mean RV of each order again weighted by RMS^{-2}. For each exposure, we then generate a coadded RV using weights w determined by the RV information content in each order,[17] which includes the
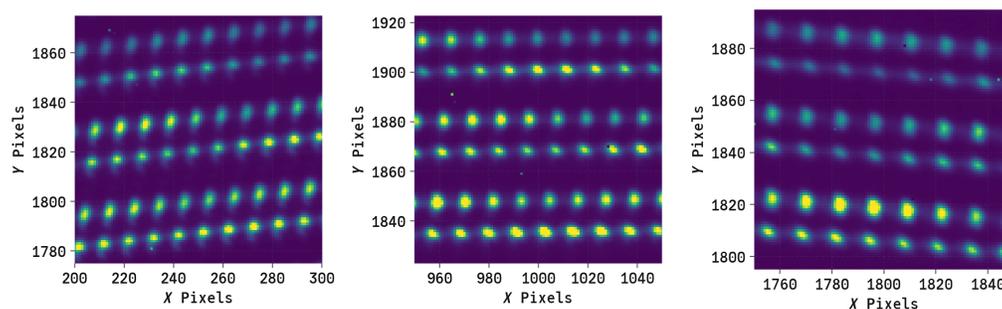

Fig. 2 Raw PARVI frame of the LFC injected through the science (top) and calibration (bottom) fibers. We show the same three orders $m = 89$ to 91 across the detector (top to bottom; wavelength increases from left to right). The tilt in the PSF is different for the two fibers and changes across each order (and orders). The colormap is arbitrarily scaled for adequate contrast.
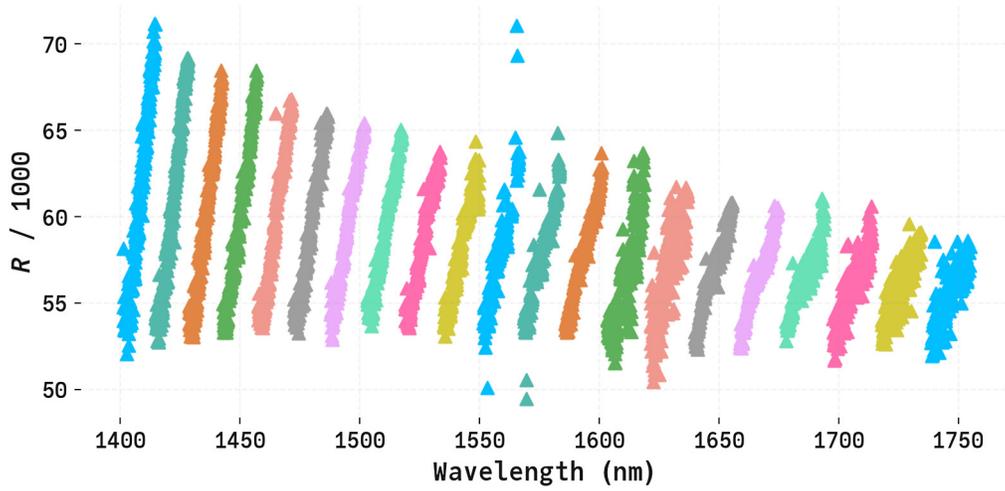
Fig. 3 With triangular markers, we show the spectral resolution $R = \lambda/\Delta\lambda$ as measured by fits to individual 1D LFC modes. Each like-color corresponds to a like-order ($m = 85$ to 105). Due to PARVI's compact construction, the effective spectral resolution of the 1D spectrum changes by $\approx 20\%$ within an order.

measured S/N of the observation and is highest in the presence of a strong signal and "sharp" (i.e., narrow) stellar features

$$\sigma_{\mathrm{RV}} = c \left[\sum_i \left(\frac{\lambda_i^2 S_i^2}{A_i} \right) \right]^{-1/2},$$

$$S_i = \frac{\mathrm{d}I_\star}{\mathrm{d}\lambda_i} I_t(\lambda_i) I_c(\lambda_i),$$

$$A_i = I_\star(\lambda_i) I_t(\lambda_i) I_c(\lambda_i),$$

$$w = \frac{1}{\sigma_{\mathrm{RV}}^2 \mathrm{RMS}^2}, \tag{1}$$

where $I_\star$, I_t, and I_c are the stellar template, telluric template, and best-fit continuum model, respectively, in normalized units, and c is the speed of light. The derivative of the stellar spectrum is computed by representing the template as a cubic spline. The stellar and telluric templates are further convolved according to the nominal LSF model. Equation (1) is computed and summed over the detector grid.

We find nearly identical results for both sets of spectra. The median RMS from the spectral model fitting is 0.69%, and the median coadded RV error (per-exposure) is 7.5 m s^{-1}. Example fits from the initial and final iterations are shown in Fig. 4. In Fig. 5, we show the measured RV errors for all exposures for individual orders and binned across orders, and the corresponding theoretical noise floor calculated with Eq. (1). For both the individual order and binned RVs, the attained precision is $\sim$30% to 50% worse than the theoretical curves predict. This may indicate that changes in the wavelength solution over the four nights are appreciably chromatic (in velocity). Our ability to accurately model the other spectral components (namely tellurics) may also contribute to this discrepancy. We find no correlation between the average signal-to-noise ratio and seeing or airmass for these observations, indicating that either variable weather conditions (e.g., clouds, seeing) or fiber coupling with P3K are primarily responsible for the changes in throughput.

5 Results

5.1 RM Signal of HD 189733 b

Here, we analyze the RVs from UT May 15 where we attempt to detect the RM signal of HD 189733 b. When a planet transits its host star, there is break in symmetry of the receding versus approaching limbs of the star. This manifests as an artificial Doppler shift in the stellar spectrum,
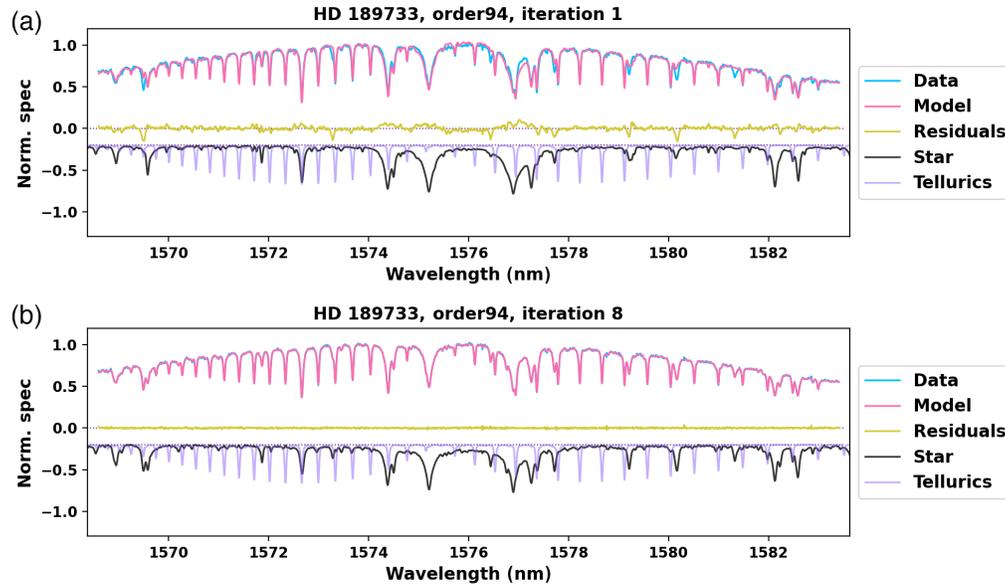
Fig. 4 (a) Example spectral model fit for order $m = 94$ using a purely synthetic stellar spectrum. (b) The same fit for the final iteration[10] after updating the stellar template based on the residuals from fits for all observations (Sec. 4).
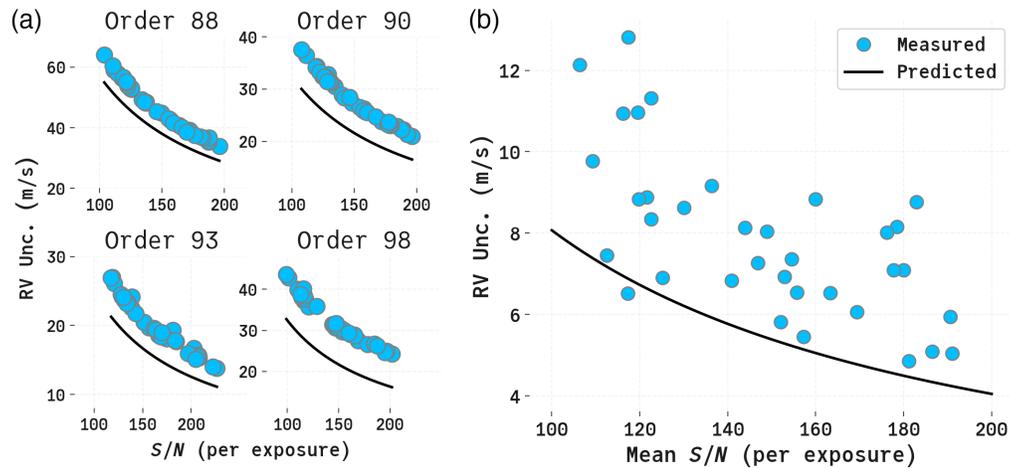

Fig. 5 (a) Per-exposure measured RV errors plotted against the average S/N-per 1D spectral pixel (1 resolution element ≈ 3.5 spectral pixels for $R = 60{,}000$, the approximate resolution for these extracted spectra) for all observations of HD 189733 with PARVI. All exposure times are identical (372 s), but the S/N varies due to variable seeing, fiber coupling, and the airmass of the observation. In black, we plot the theoretical noise floor [Eq. (1)]. (b) Same, but for a subset of individual orders. Orders $m = 88$ and $m = 93$ represent the orders with the lowest and largest RV information content, respectively.

and such measurements can be used to determine the star's projected spin-orbit obliquity angle β.[18,19]

We measure β using the Python package starry,[20] which generates both the orbital and RM RV components. Due to the lack of sufficient orbital phase coverage on this single night, we only fit for β and an RV offset, γ. We make use of a linear limb-darkening coefficient C_1 calculated from the exoplanet characterization toolkit (ExoCTK; Ref. 21) with a top-hat bandpass corresponding to the PARVI echelle orders considered in this analysis. Remaining orbital and RM parameters are fixed to the values provided in Ref. 22. The model is optimized by minimizing the reduced chi-squared statistic (χ^2_{red}) with lmfit (https://lmfit.github.io/lmfit-py/index.html).[23] lmfit
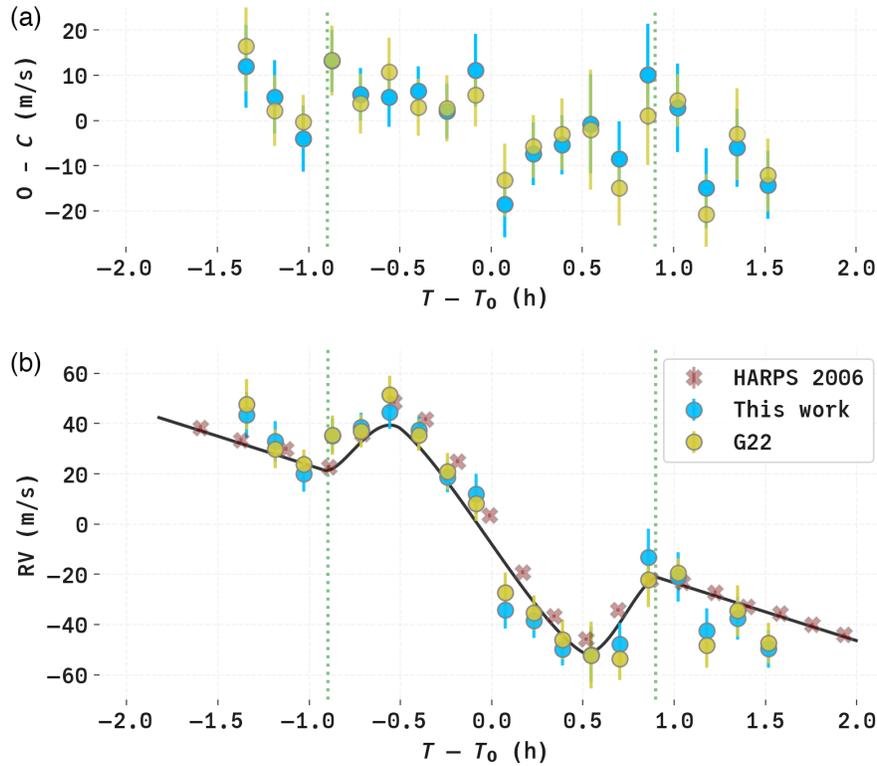
Fig. 6 RM signal of HD 189733 b. (a) We plot both sets of PARVI RVs and an example of a corresponding best-fit RM model in black (Table 2, column 2). In maroon, we plot HARPS RVs from 2006.[22] Ingress start and egress end are marked as vertical dashed green lines. Transit epoch information is generated from the NASA exoplanet archive transit prediction tool.[24] (b) The corresponding residuals for the PARVI RVs.

also provides parameter uncertainties via finite difference techniques. We find similar results for the three sets of RVs, each deviant by ≈ 1 to 2σ from a previous detection with high accuracy radial velocity planet searcher (HARPS) (e.g., $\beta = 0.85^{+0.32}_{-0.28}$ deg, Ref. 22) but still consistent with an aligned orbit. This result further demonstrates our method of retrieving the stellar spectrum and forward modeling the observation (Sec. 4) is sensitive to non-"Doppler-like" distortions in the stellar spectrum. We suspect the birefringence-induced instabilities are the primary source of the correlated structure in the residuals of Fig. 6; however, this is difficult to discern when using a data-driven stellar template with so few observations and limited barycentric sampling. The PARVI RVs and best-fit RM models are shown in Fig. 6. A summary of parameters is provided in Table 2.

5.2 Detection of Molecular Species

The atmosphere of HD 189733 b has been explored in detail, making it an optimal target to test the capabilities of PARVI. Evidence for H_2O was first reported by Ref. 26 using Spitzer IRAC transit photometry. This detection was later confirmed, and Birkby et al.[27] found evidence for H_2O with CRIRES on the 8.2 m VLT while[28] presented HST WFC3 transmission spectroscopy that showed clear H_2O molecular bandheads. Later, Brogi et al.[29] and Alonso-Floriano[30] both demonstrated that analysis techniques using high-resolution spectroscopy had improved to a point where H_2O was confidently detected with 3.5 m class ground-based telescopes (GIANO and CARMENES, respectively). In addition to H_2O, molecular absorption from CO at 2.3 μm was detected by Brogi et al.,[31] and evidence for HCN[32] and CH_4[33] have also been observed in the atmosphere of HD 189733 b.

Due to the similarity in wavelength coverage, spectral resolution, and molecules searched for, we followed a similar overall analysis procedure as Ref. 30. As is common, we kept the orders separate during the whole analysis procedure so that we could isolate important parts of the spectrum and did not perform any unnecessary interpolation. The following steps were

Table 2 Summary of the parameters (top: optimized, bottom: fixed) used to model the composite orbital + RM signal of HD 189733 b in Sec. 5.1.

Name	Opt. value (this work)	Opt. value (Ref. 9)	Opt. value (this work, dynamic LSF)
β (deg)	-8.6 ± 5.5	-6.8 ± 5.1	-8.5 ± 5.9
γ (m s^{-1})	-22.9 ± 3.4	-25.6 ± 3.0	-21.8 ± 3.5
	1.66	1.42	1.86

Name	Value	Citation
P_b (days)	2.218575200	
(BJD)	2459714.9479	
i_b (deg)	85.508	
M_b ($M_\oplus$)	362	
$v_\star \sin i$ (km s^{-1})	3.316	22
$R_\star$ ($R_\odot$)	0.78	
$M_\star$ ($M_\odot$)	0.84	
e_b	0	
$\omega_b^\star$ (rad)	π	25
C_1	0.64	21

BJP, barycentric Julian date.

performed for orders $m = 85$ to 105 and then the resulting cross correlation grids were combined after. Using the reduced spectra presented in Sec. 3, we created an $M \times N$ array with the spectra, where the M rows are each sorted by wavelength, and the N columns are sorted by the time of the observation. Any columns that had on average <20% transmittance through the atmosphere due to telluric absorption were masked. We then performed standard spectral cleaning steps, including normalization, sigma clipping, and the application of a high-pass filter with a width of 100 pixels. As the star remains relatively stationary in time while the planet's spectrum experiences large RV shifts, we divided each spectrum by the average spectrum in time to remove the stellar signal while leaving the planet's signal intact. Finally, we down-weighted any pixel columns that had large variances and hence were noisier, by dividing by the standard deviation of each column.

At this stage, we were still left with significant telluric residuals, as the shape and depth of the telluric features change throughout the night. However, the telluric variations are relatively constant in velocity and usually slowly vary over time due to airmass changes. Principle component analysis (PCA) or SYSREM (which applies PCA with varying uncertainties) have become the standard methods for removing these slowly varying linear trends in high-resolution transmission and emission observations (e.g., Refs. 30, 34, and 35). Following these standard methods, PCA is iteratively applied to the cleaned time series spectra, and each iteration is subtracted to remove any linear trends. As discussed in Ref. 34, applying too many PCA iterations can begin to remove the planet's signal. We therefore chose to use a conservative five PCA iterations, as we found that at this point, the vast majority of the telluric residuals were removed (when plotted the data did not show any clear telluric/linear trends by eye) and using more iterations we risked removing part of the planet's signal.

To detect the planet's signal within the noise, we cross correlated each cleaned and detrended spectrum with a model of the planet's atmosphere, which was made using petitRADTRANS.[36] We made a different model for each molecule, including H_2O, HCN, NH_3, CO, and CH_4 (see Fig. 7). As input to the code, we used the planet's parameters and temperature pressure profile from Ref. 29. When available, we used previously measured
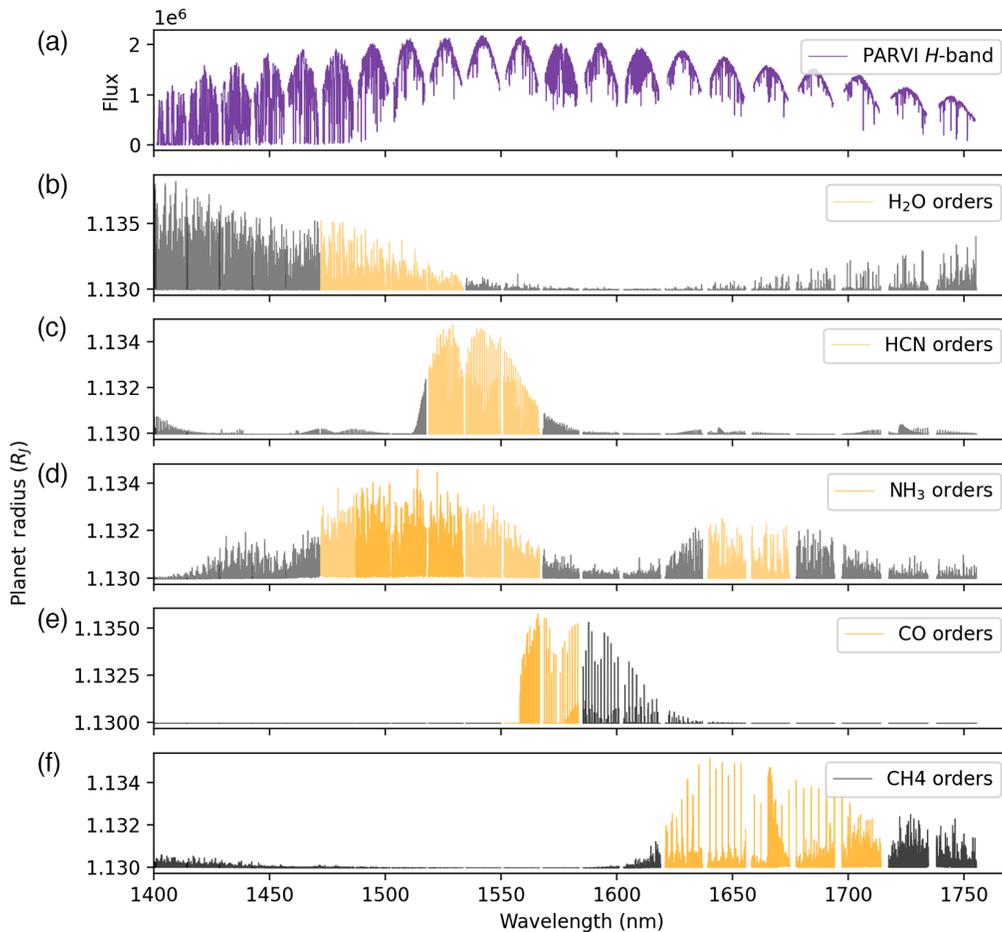
Fig. 7 (a) All of the orders of a single PARVI spectrum for HD 189733. (b)–(f) Models of H_2O, HCN, NH_3, CO, and CH_4, created using petitRADTRANS, and interpolated onto the same wavelength grid as the data. The gold highlighted orders show which orders we selected to combine for our cross correlation analyses for each molecule. These orders were chosen using injection and recovery tests.

abundances of 3×10^{-3} for CO,[37] and 5×10^{-4} for H_2O,[38] and the tentative detection with a best fit abundance of 10^{-6} for HCN. Otherwise, we implemented the equilibrium chemistry code described in Ref. 39 to estimate volume mixing ratios of 10^{-5} and 10^{-6} for NH_3 and CH_4, respectively. We nominally chose a cloud opacity deck at 10^{-2} bars. We varied both the cloud deck and abundances but did not find any significant differences in the reported signal strengths.

We created cross correlation grids for each order and then combined these by simply averaging together the orders chosen for each molecule (see Fig. 7 to see which orders were chosen for each molecule). We performed injection and recovery tests to decide which orders to include. In general, the orders that produced a detectable signal did not contain too many saturated telluric lines, did not lie at the very edge of the detector, and exhibited strong opacity from the specified molecule. We chose to not weight the orders when we combined them because this process has been shown to incorrectly inflate the detection significance.[32]

For all of the species besides H_2O, we only use H band orders ($m = 85$ to 105) due to the higher precision of the wavelength solution in this region. We tentatively detect H_2O and CO, both with $S/N \sim 4$. These two molecules have both been confidently detected at high spectral resolution in this planet by previous studies using a variety of instruments,[27,29–31] and so our detections of these species and non-detections of the others (all of which are expected to have lower abundances and have not been confidently detected by high-resolution atmospheric studies) further adds confidence to our tentative signals (Fig. 8).
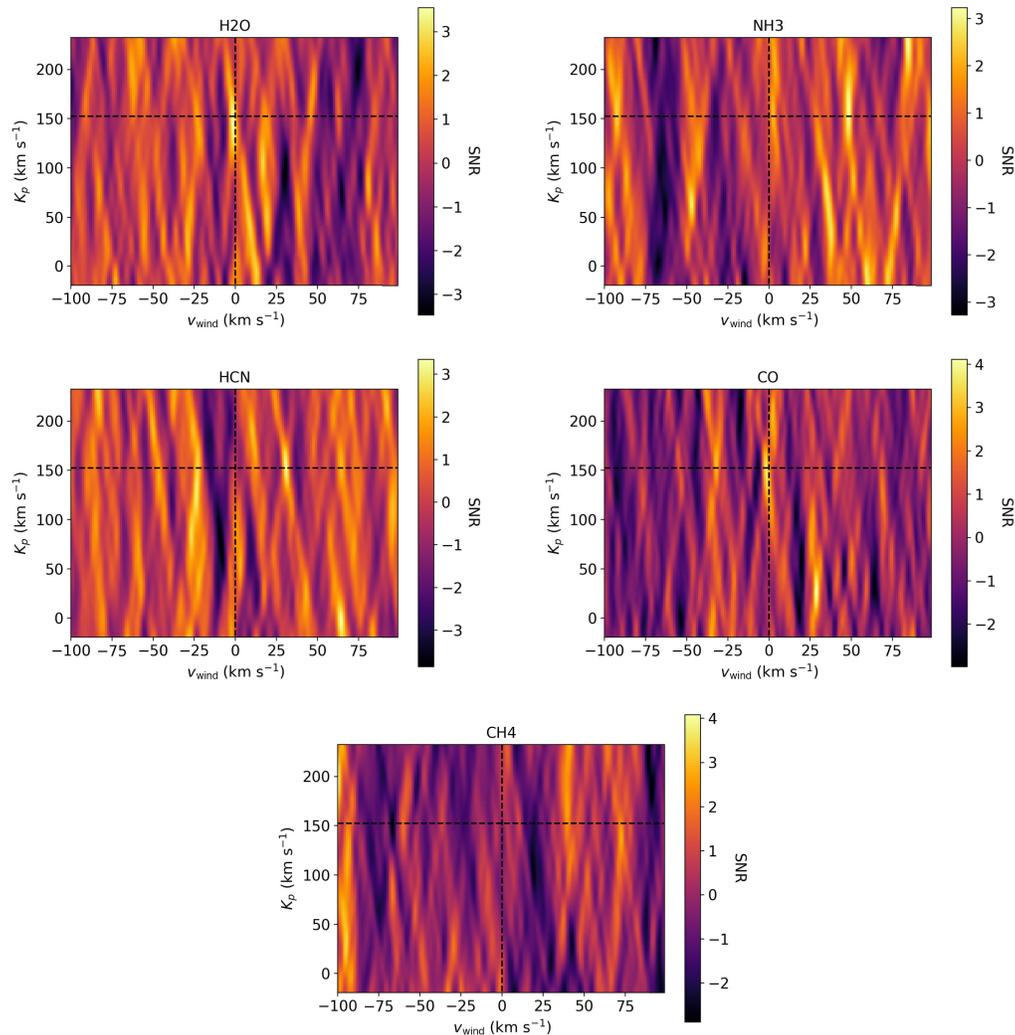
Fig. 8 Marginal detections of H_2O with $S/N = 3.9$ using four orders of PARVI data near the 1400 nm H_2O bandhead, and CO with a $S/N = 4.1$ using two orders near the 1600 nm bandhead. We do not detect any evidence of HCN, NH_3, or CH_4.

6 Limitations and Ongoing Improvements

6.1 Hardware Improvements

PARVI's epoch-to-epoch RV precision has been limited by wavelength instability due to an interaction between the time-varying polarization state of the input fiber-fed light with a small parasitic birefringence in the spectrograph's silicon cross-disperser. Silicon is an isotropic crystal and is not expected to have axially dependent refractive indices, so this birefringence possibly arises from mounting stresses at cryogenic temperature. The result is a polarization dependent (primarily tilt) aberration, which results in a tiny separation (0.02 pixel) of the PSFs of the 2 polarization states. Since the LFC modes are intrinsically highly polarized and since this polarization state changes in time due to thermal and elasto-optical changes in the input fiber, apparent centroid shifts in LFC modes are observed. Starlight carrying fibers from the telescope experience strong elasto-optical agitation (especially during slews); however, the starlight is only mildly polarized, mainly due to upstream optical reflections. The net result is that the source and LFC calibration light are shifted differentially by the silicon prism, and therefore, we cannot rely on the simultaneous LFC trace to provide an accurate new wavelength solution for each science exposure. Specifically, we find the birefringent properties of the cross-dispersing optic are responsible for RV errors on the order of 10 m s^{-1}.[6] These errors are chromatic with a

wavelength span comparable to an echelle order, and do not average out across multiple orders. The timescale of this instability is on the order of a typical exposure ($\sim$5 minutes) and is likely a major source of correlated errors in Fig. 6. Significant work has been ongoing to characterize and mitigate this polarization-noise through scrambling the polarization state of both the starlight and calibration signals; we do not expect this to impact future observations.[6] However, because the majority of RV observations presented in this work are from a single night with no telescope slews (only telescope tracking), we find the relative precision within the science trace alone to be sufficiently demonstrative of SMF Doppler spectroscopy in the context of PARVI. We expect datasets which span multiple telescope slews (i.e., multiple nights) will be more severely impacted by this effect.

We remind the reader that these results are attained by only utilizing the red half ($m = 85$ to 99, $\lambda \sim 1488$ to 1755 nm) of the available spectral coverage due to the limited spectral coverage of the LFC. Echelle orders $m = 100$ to 110 ($\lambda \sim 1336$ to 1486) are highly contaminated by telluric water absorption; however, the remaining orders ($m = 111$ to 129, $\lambda \sim 1137$ to 1336) are relatively sparse in telluric features yet rich in stellar features, especially for late K and M stars (similar to H band, e.g., Ref. 40). We are exploring the utility of multiple absorption gas cells (hydrogen fluoride, methane, and a quad cell with 12CO, 13CO, C2H2, and H2O) and a SANTEC TL-570 high performance tunable laser[41] to provide a wavelength reference in the J band.

6.2 Software Improvements

One significant difference between our spectral extraction and Ref. 9 is the formulation of the PSF. In this work, we generate a 1D (vertical) PSF unique to each echelle order according to the median of the normalized data within an order. In Ref. 9, a 1D PSF is calculated using a coadded fiber-flat image. For a given order, each column is independently fit with a Gaussian function, and the nominal Gaussian widths are used to generate a 1D profile for each column, which is inherently chromatic. Specifically, we find the width in the cross-dispersion direction of the effective 1D PSF changes by $\sim$20% across an order.

Most spectral extraction routines treat the PSF as a 1D function and extract columns individually. However, the image of the fibers for nearly all high resolution echelle spectrographs are evidently two-dimensional, and the effective spectral resolution of the extracted spectrum is therefore degraded according to the deviation of the observed PSF relative to the effective PSF of the echelle grating at native resolution. Both spectral extraction routines considered in this work treat the PSF as a 1D entity, and are therefore subject to this loss in spectral resolution (see Fig. 2). Specifically, a tilt of 45° degrades the resolution by a factor of $\approx\sqrt{2}$ using a vertical extraction algorithm. In our analyses, we find the spectral resolution R varies from 50,000 to 65,000 (Fig. 3), which is less than the designed resolution of $R \gtrsim 87,000$ (Table 1) and may also be due to manufacturing and/or focusing errors. We find the 1D width of LFC modes to be $\approx$15% larger in 2022 compared to 2021 due to service operations between observing semesters (PARVI has been opened several times during commissioning since 2019 to determine the source of birefringence induced instability and to implement various upgrades.) and is further limiting the obtained resolution for these observations.

PARVI echellograms are therefore an excellent test-case for "spectro-perfectionism" (SP; Refs. 42 and 43), where the spectrum is extracted by explicitly deconvolving the image according to a 2D PSF, which can further capture chromatic dependence of the PSF shape. With an accurate 2D model of the PSF, the application of SP should result in a higher spectral resolution for the 1D spectrum. A second advantage of SP is that it provides a means by which to generate a matrix that describes the convolution of the 1D spectrum with an effective LSF by diagonalizing the matrix describing the covariance between extracted points. This "re-convolution" matrix can then be used to convolve any theoretical spectral model (at an effective infinite resolution) to match the resolution obtained through SP extraction. The effective LSF's of this design matrix (e.g., the matrix rows) may be chromatic if that is what the data supports. We are actively developing and testing the application of SP extraction for PARVI data to take advantage of the full spectral resolution.

For the majority of targets, we will coadd the RVs from different exposures together within a given night to improve our precision for that target. In the case of HD 189733 (and for targets

with events/processes on similar timescales), we keep exposures separated because the change in the apparent (RM and orbital) stellar RV between exposures is larger than our measurement uncertainties.

7 Conclusion

Next-generation spectrographs are utilizing innovative technologies to overcome the current limitations of Doppler precision. PARVI is one such high-resolution NIR spectrograph on the 200 inch Hale telescope at Palomar Observatory. By utilizing SMFs, PARVI offers several advantages compared with other spectrographs including a much smaller optical configuration for a given spectral resolution. In this work, we have demonstrated PARVI's Doppler performance and high spectral resolution capabilities at H band wavelengths. We present our data processing routines in Secs. 3 and 4. We have detected the RM signal of the transiting planet HD 189733 b and find consistent results with previous observations in Sec. 5.1. In Sec. 5.2, we also confirm the presence of H_2O and CO in the atmosphere of HD 189733 b via transmission spectroscopy.

With improved Doppler stability and characterization, higher throughput, and a higher resolution spectrum provided through a more sophisticated spectral extraction algorithm (SP extraction, Sec. 6.2), we anticipate the PARVI Doppler performance to approach the design goal of ~1 m s^{-1} for moderately bright late-type stars. Finally, we note that the insights obtained from designing, constructing, and testing a first-of-its-kind instrument, such as PARVI, help inform next-generation spectrographs utilizing SMFs (e.g., iLocator,[44] Keck planet imager and characterizer (KPIC),[45] the high resolution infrared spectrograph for exoplanet characterization,[46] and EarthFinder).[47]

8 Appendix: Spectral Extraction

In the descriptions that follow, we adopt the convention that spectral orders are (nearly) aligned (parallel-to) with detector rows. A background-subtraction with a high S/N dark frame is first performed to remove dark current and any leaked light scattered within the spectrograph, followed by a flat-field division to correct for pixel-to-pixel variations with the detector fully-illuminated. Images of the fiber-flat are used to provide preliminary locations of the traces on the detector.

We first refine the trace positions based on a sixth-degree polynomial fit to the centroids of each detector column, denoted by $y_c(x)$. Masked pixels are filled via bilinear interpolation to yield unbiased centroids. We then normalize each detector column such that the total signal per-column is unity. We generate a 1D (vertical) trace profile using a least-squares cubic spline fit with the SciPy[48] routine scipy.interpolate.LSQUnivariateSpline. The fit is performed in log-space to prohibit negative values in the profile. Each column's y-positions are corrected according to $y_c(x)$. This method of retrieving the profile weights requires no resampling of the data and results in an analytic continuous curve that may be trivially sampled.

Spectra are then extracted in an iterable fashion. For a given column, the trace profile (cubic spline) is shifted and sampled onto the detector grid by explicitly integrating over a given detector pixel. To extract a column x, we then minimize

$$\mathcal{F} = \sum_y w_{xy}(S_{xy} - A_x P_{xy})^2, \tag{2}$$

where A_x is a scale factor to match the profile P to the data column S. Equation (2) can be solved linearly for A_x

$$A_x = \frac{\sum_y w_{xy} S_{xy} P_{xy}}{\sum_y w_{xy} P_{xy}^2}. \tag{3}$$

The weights w_{xy} are chosen according to a pixel noise model; $w_{xy} = M_{xy}/v_{xy}$, where M_{xy} is a binary mask, and v_{xy} is the variance. v_{xy} includes S_{xy} on a first sub-iteration and is substituted

with $f_x P_{xy}$ on four (arbitrarily chosen) subsequent sub-iterations. v_{xy} further includes the read-out-noise of the H2RG detector. The final flux is then determined by the profile and nominal scale factor

$$f_x = A_x \int_{-b}^{b} P(x, y)\mathrm{d}y, \tag{4}$$

where the integral is computed by explicitly integrating the cubic spline representation of P. A detector pixel is only considered in the fit [Eqs. (2)–(3)] if it will contribute to the extracted flux. We set the half-aperture size $b = 5$ pixels.

Finally, we smooth the extracted 1D spectrum with a three-pixel wide median filter, and reconvolve this smoothed spectrum back onto the 2D detector grid. Outliers are identified as 4-σ deviant in the normalized residuals

$$r_{xy} = \frac{S_{xy} - I_{xy}}{\sqrt{I_{xy} + \mathrm{RON}^2}}, \tag{5}$$

where S_{xy} and I_{xy} represent the data and smoothed 2D model, respectively. These steps are repeated until no deviant pixels are identified, typically requiring 3 to 10 iterations. Finally, we note this extraction process is equivalent to common "optimal" spectral extraction routines (e.g., Refs. 49–51), up to the determination and normalization of the profile P.

Data and Code Availability

All data processed in this work are available from the authors upon request. All codes developed for this work are publicly available at https://github.com/astrobc1.

References

1. N. E. Batalha et al., "The precision of mass measurements required for robust atmospheric characterization of transiting exoplanets," *Astrophys. J. Lett.* **885**, L25 (2019).
2. National Academies of Sciences, Engineering, and Medicine, *Exoplanet Science Strategy*, The National Academies Press, Washington, DC (2018).
3. X. Yi et al., "Demonstration of a near-IR line-referenced electro-optical laser frequency comb for precision radial velocity measurements in astronomy," *Nat. Commun.* **7**, 10436 (2016).
4. S. Halverson et al., "An efficient, compact, and versatile fiber double scrambler for high precision radial velocity instruments," *Astrophys. J.* **806**, 61 (2015).
5. A. J. Bechter et al., "Mitigation of polarization effects in single-mode fiber spectrographs," *Publ. Astron. Soc. Pac.* **132**, 095001 (2020).
6. R. K. Gibson et al., "The accordion effect: a consequence of polarized light in precision radial velocity spectrometers," in preparation.
7. F. Bouchy et al., "ELODIE metallicity-biased search for transiting Hot Jupiters. II. A very hot Jupiter transiting the bright K star HD 189733," *A&A* **444**, L15–L19 (2005).
8. R. K. Gibson et al., "Characterization of the C-RED 2: a high-frame rate near-infrared camera," *J. Astron. Telesc. Instrum. Syst.* **6**, 011002 (2020).

9. K. R. Gibson et al., "Data reduction pipeline and performance for the Palomar radial velocity instrument," *J. Astron. Telesc. Instrum. Syst.* **8**, 038006 (2022).

10. R. Brahm, A. Jordán, and N. Espinoza, "CERES: a set of automated routines for echelle spectra," *Publ. Astron. Soc. Pac.* **129**, 034002 (2017).

11. B. Cale et al., "Precise radial velocities of cool low-mass stars with iSHELL," *Astron. J.* **158**, 170 (2019).

12. P. K. Mogensen et al., "JuliaNLSolvers/NLsolve.jl: v4.5.1 (v4.5.1)," *Zenodo* (2020).

13. G. M. Brandt, T. D. Brandt, and C. McCully, "Automatic Échelle spectrograph wavelength calibration," *Astron. J.* **160**, 25 (2020).

14. J. L. Bertaux et al., "TAPAS, a web-based service of atmospheric transmission computation for astronomy," *A&A* **564**, A46 (2014).

15. F. Allard, "The BT-settl model atmospheres for stars, brown dwarfs and planets," in *Exploring the Formation and Evolution of Planetary Systems, Proc. Int. Astronom. Union, IAU Symp.*, M. Booth, B. C. Matthews, and J. R. Graham, Eds., Vol. **299**, pp. 271–272 (2014).

16. S. Czesla et al., "PyA: Python astronomy-related packages," (2019).

17. C. Lovis and D. Fischer, "Radial velocity techniques for exoplanets," in *Exoplanets*, S. Seager, Ed., pp. 27–53, University of Arizona Press, Tucson, AZ (2010).

18. Y. Hosokawa, "On the rotation effect of velocity curves in eclipsing binary systems," *Publ. Astronom. Soc. Japan* **5**, 88 (1953).

19. A. Giménez, "Equations for the analysis of the Rossiter-McLaughlin effect in extrasolar planetary transits," *Astrophys. J.* **650**, 408–413 (2006).

20. R. Luger et al., "Starry: analytic occultation light curves," *Astron. J.* **157**, 64 (2019).

21. M. Bourque et al., "The exoplanet characterization toolkit (ExoCTK)," (2021).

22. A. H. M. J. Triaud et al., "The Rossiter-McLaughlin effect of CoRoT-3b and HD 189733b," *A&A* **506**, 377–384 (2009).

23. M. Newville et al., "LMFIT: non-linear least-square minimization and curve-fitting for Python," *Zenodo* (2014).

24. R. L. Akeson et al., "The NASA exoplanet archive: data and tools for exoplanet research," *Publ. Astron. Soc. Pac.* **125**, 989–999 (2013).

25. NASA Exoplanet Archive, "Confirmed planets table," (2019).

26. C. J. Grillmair et al., "A spitzer spectrum of the exoplanet HD 189733b," *Astrophys. J. Lett.* **658**, L115–L118 (2007).

27. J. L. Birkby et al., "Detection of water absorption in the day side atmosphere of HD 189733 b using ground-based high-resolution spectroscopy at 3.2 μm," *MNRAS* **436**, L35–L39 (2013).

28. P. R. McCullough et al., "Water vapor in the spectrum of the extrasolar planet HD 189733b. I. The transit," *Astrophys. J.* **791**, 55 (2014).

29. M. Brogi et al., "Exoplanet atmospheres with GIANO. I. Water in the transmission spectrum of HD 189 733 b," *A&A* **615**, A16 (2018).

30. F. J. Alonso-Floriano et al., "Multiple water band detections in the CARMENES near-infrared transmission spectrum of HD 189733 b," *A&A* **621**, A74 (2019).

31. M. Brogi et al., "Rotation and winds of exoplanet HD 189733 b measured with high-dispersion transmission spectroscopy," *Astrophys. J.* **817**, 106 (2016).

32. S. H. C. Cabot et al., "On the robustness of analysis techniques for molecular detections using high-resolution exoplanet spectroscopy," *MNRAS* **482**, 4422–4436 (2019).

33. M. R. Swain, G. Vasisht, and G. Tinetti, "The presence of methane in the atmosphere of an extrasolar planet," *Nature* **452**, 329–331 (2008).

34. J. L. Birkby et al., "Discovery of water at high spectral resolution in the atmosphere of 51 Peg b," *Astron. J.* **153**, 138 (2017).

35. A. Y. Kesseli et al., "A search for FeH in hot-jupiter atmospheres with high-dispersion spectroscopy," *Astron. J.* **160**, 228 (2020).

36. P. Mollière et al., "petitRADTRANS. A Python radiative transfer package for exoplanet characterization and retrieval," *A&A* **627**, A67 (2019).

37. M. Brogi and M. R. Line, "Retrieving temperatures and abundances of exoplanet atmospheres with high-resolution cross-correlation spectroscopy," *Astron. J.* **157**, 114 (2019).

38. A. Boucher et al., "Characterizing exoplanetary atmospheres at high resolution with SPIRou: detection of water on HD 189733 b," *Astron. J.* **162**, 233 (2021).

39. P. Mollière et al., "Observing transiting planets with JWST. Prime targets and their synthetic spectral observations," *A&A* **600**, A10 (2017).

40. A. Reiners et al., "The CARMENES search for exoplanets around M dwarfs. High-resolution optical and near-infrared spectroscopy of 324 survey stars," *A&A* **612**, A49 (2018).

41. https://inst.santec.com/products/tunablelaser/tsl-570.

42. A. S. Bolton and D. J. Schlegel, "Spectro-perfectionism: an algorithmic framework for photon noise-limited extraction of optical fiber spectroscopy," *Publ. Astron. Soc. Pac.* **122**, 248 (2010).

43. M. A. Cornachione et al., "A full implementation of spectro-perfectionism for precise radial velocity exoplanet detection: a test case with the MINERVA reduction pipeline," *Publ. Astron. Soc. Pac.* **131**, 124503 (2019).

44. J. Crass et al., "iLocater—the final steps in delivering an EPRV instrument for the LBT," in *Amer. Astron. Soc. Meeting Abstracts*, January, Vol. 55, p. 267.05 (2023).

45. J.-R. Delorme et al., "Keck planet imager and characterizer: a dedicated single-mode fiber injection unit for high-resolution exoplanet spectroscopy," *J. Astron. Telesc. Instrum. Syst.* **7**, 035006 (2021).

46. D. Mawet et al., "High-resolution infrared spectrograph for exoplanet characterization with the keck and thirty meter telescopes," *Bull. Am. Astron. Soc.* **51**, 134 (2019).

47. P. Plavchan et al., "EarthFinder probe mission concept study: characterizing nearby stellar exoplanet systems with earth-mass analogs for future direct imaging," arXiv:2006.13428 (2020).

48. P. Virtanen et al., "SciPy 1.0: fundamental algorithms for scientific computing in Python," *Nat. Methods* **17**, 261–272 (2020).

49. K. Horne, "An optimal extraction algorithm for CCD spectroscopy," *Publ. Astron. Soc. Pac.* **98**, 609–617 (1986).

50. T. R. Marsh, "The extraction of highly distorted spectra," *Publ. Astron. Soc. Pac.* **101**, 1032 (1989).

51. M. Zechmeister, G. Anglada-Escudé, and A. Reiners, "Flat-relative optimal extraction. A quick and efficient algorithm for stabilised spectrographs," *A&A* **561**, A59 (2014).

Biographies of the authors are not available.